Phase imaging using shifted wavefront sensor images

Zhengyun Zhang,[1,*] Zhi Chen,[1,2] Shakil Rehman,[1,2] and George Barbastathis[1,2,3,4]

[1]*BioSyM IRG, Singapore-MIT Alliance for Research and Technology (SMART) Centre, 1 CREATE Way,
#04-13/14 Enterprise Wing, Singapore 138602, Singapore*

[2]*CENSAM IRG, Singapore-MIT Alliance for Research and Technology (SMART) Centre, 1 CREATE Way,
#09-03 CREATE Tower, Singapore 138602, Singapore*

[3]*Department of Mechanical Engineering, Massachusetts Institute of Technology, 77 Massachusetts Avenue,
Cambridge, Massachusetts 02139, USA*

[4]*University of Michigan-Shanghai Jiao Tong University Joint Institute, 800 Dong Chuan Road, Shanghai, 200240, China
Corresponding author: zhengyun@smart.mit.edu

We propose a new approach to the complete retrieval of a coherent field (amplitude and phase) using the same
hardware configuration as a Shack–Hartmann sensor but with two modifications: first, we add a transversally shifted
measurement to resolve ambiguities in the measured phase; and second, we employ factored form descent (FFD), an
inverse algorithm for coherence retrieval, with a hard rank constraint. We verified the proposed approach using both
numerical simulations and experiments.   © 2014 Optical Society of America

OCIS codes: (100.5070) Phase retrieval; (010.7350) Wave-front sensing; (100.3190) Inverse problems.
http://dx.doi.org/10.1364/OL.39.006177

Knowledge of the phase of a coherent field has many applications in optics and imaging, but at optical frequencies and above, phase can only be inferred through intensity measurements. Hence, many methods have been developed to shape the intensity for phase retrieval, e.g., holography [1–6], wavefront sensing with lens arrays [7–11], iterative projections [12,13], transport-of-intensity equation (TIE) methods [14,15], ptychography [16–18], and quantitative differential interference contrast (DIC) imaging [19]. Recent lens array imaging papers [9–11] adopt iterative algorithms instead of classic centroid-based reconstruction to exploit the additional information contained in the *structure* of the intensity behind each lenslet. However, they still impose strong restrictions on the field—while centroid-based reconstruction methods assume an extremely smooth phase profile, these iterative methods employ smooth basis functions with large spatial support (i.e., Zernike polynomials and vortex modes). Without these restrictions, straightforward inversion can yield spurious phase discontinuities at lenslet boundaries due to noise, since a single wavefront sensor image lacks information on the relative phase of portions of the field captured by different lenslets [11].

We instead propose taking a second measurement after transversally shifting the lens array diagonally so that lenslet centers in one image coincide with lenslet corners in the other. Nearby points in the field from adjacent lenslets in the first image now fall within the same lenslet in the second, their interference yielding information on their relative phase. This additional information relaxes restrictions on the field, enabling the use of arbitrary basis functions. For versatility and computational convenience, we will use *sinc* basis functions corresponding to Nyquist sampling with a square sampling lattice.

Our actual inversion algorithm retrieves the phase and amplitude of the coherent field from this set of wavefront sensor images. It is based on factored form descent (FFD) [20], a coherence retrieval algorithm that computes the coherence modes of a partially coherent field given a linear operator description of a known optical system and measured intensity values through said optical system. We adapt FFD to the problem of coherent field retrieval by imposing a hard rank constraint; this is accomplished by modifying the merit function to allow only a single mode:

$$\hat{f}(\boldsymbol{x}) = \sum_{m=1}^{M} \sigma_m^{-2}(y_m - \boldsymbol{k}_{\boldsymbol{m}}^{\mathsf{H}}\boldsymbol{x}\boldsymbol{x}^{\mathsf{H}}\boldsymbol{k}_{\boldsymbol{m}})^2, \tag{1}$$

where M is the number of measured intensities, σ_m is an estimate of the noise standard deviation, y_m is the mth measurement, $\boldsymbol{k}_{\boldsymbol{m}}$ models the linear propagation of light from the source to the measurement position, and $\boldsymbol{x} \in \mathbb{C}^N$ is the current guess to the source field. The only difference between this formulation and classic FFD is that we replaced modes matrix X with a single mode vector $\boldsymbol{x}$. This also reduces the per-iteration computational complexity to $O(MN)$ since we only deal with a single mode instead of N of them.

Although the original FFD algorithm is a modification of a convex problem and hence has no local minima, the rank constraint modification does introduce the possibility of local minima. The true solution, being coherent, lies on the surface of the positive semi-definite cone in mutual intensity space, and the rank constraint forces the iterate to move along this surface; local minima exist when the steepest descent direction in mutual intensity space is normal to the surface. However, we have found that the modified algorithm presented here produces reliable inversion in practice given enough measurements and a good initial guess. With enough measurements, local minima only exist on the "opposite" side of the cone from the true solution. However, if the iterate starts on the "same" side of the cone, then it has no reason to land in a local minimum at the other side. A deeper study of convergence behavior is beyond the scope of this Letter, especially since the representative cases we studied
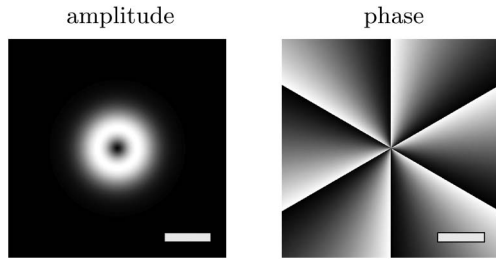
Fig. 1.   Amplitude and phase of a simulated HyGG mode. White in the amplitude image corresponds to the maximum amplitude, whereas black and white correspond to $-\pi$ and π, respectively, in the phase image. Scale bar is 0.5 mm.

yielded plausible solutions with the proposed measurement method and a flat field initial guess.

We first apply our method to recover the amplitude and phase of a simulated Hypergeometric-Gaussian (HyGG) mode [21] with parameters $p = -5$ and $m = 6$; its structural simplicity and presence of a phase vortex make it easy to verify our approach for a nontrivial yet intuitive example. The HyGG mode we simulate takes the following form:

$$U_{\mathrm{HyGG}}(r, \phi) = (r/w_0) \exp(-r^2/w_0^2 + \mathrm{j}6\phi), \qquad (2)$$

where r and ϕ are, respectively, the radial and angular spatial coordinates, $w_0 = 300$ µm is a constant determining the extent of the mode, and $\mathrm{j} = \sqrt{-1}$. The amplitude and phase of this mode are shown in Fig. 1, and we used a wavelength of 540 nm. In our simulation, this field is impinging on a wavefront sensor consisting of a lens array containing square lenslets 150 µm on a side with a 5.1 mm focal length and an imaging sensor with 500×500 pixels of 4.65 µm pitch. Two sets of images are taken with the simulated wavefront sensor, with the second set of images taken after the wavefront sensor is shifted 75 µm along each axis of the lens array lattice.

Each set contains 16 noisy images incorporating both Gaussian noise (with standard deviation equal to 0.5% of the brightest pixel) and Poisson noise (to emulate 5×10^5 total captured photons). The mean and standard deviation of each set are used as input to the modified FFD algorithm, and the recovered amplitude and phase after 500 iterations ($\sim$30 min on a modern laptop running MATLAB) are shown in Fig. 2, with convergence
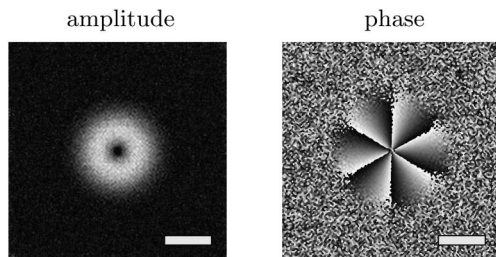

Fig. 2.   Recovered amplitude and phase of the HyGG mode from a set of wavefront sensor images emulating a total photon count of 5×10^5. White in the amplitude image corresponds to the maximum amplitude of the ground-truth, whereas black and white correspond to $-\pi$ and π, respectively, in the phase image. Scale bar is 0.5 mm.
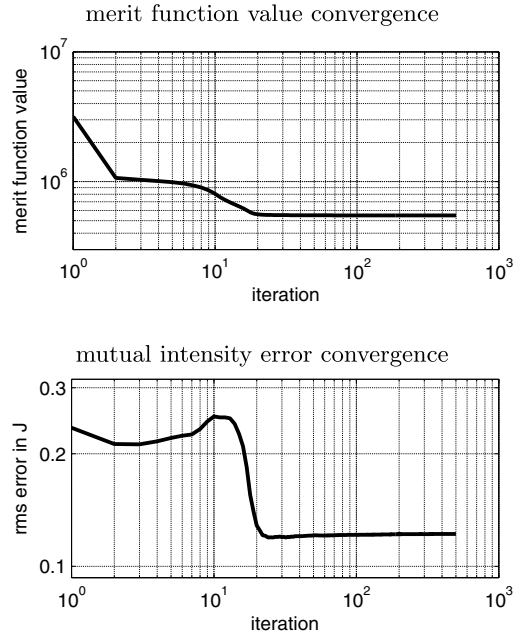

Fig. 3.   Top log–log plot shows the merit function value as a function of iteration number, and the bottom log–log plot shows the iteration-wise progression of the RMS error in mutual intensity between the current iterate and the original HyGG mode. The somewhat erratic behavior of the RMS error is due to ill-posedness and can be ameliorated by preconditioning (i.e., modifying the gradient update rule). We have chosen to defer this improvement to future work, since the current simple method still seems to work quite well in the representative situations that we examined.

plots shown in Fig. 3. The field was specified by a 129×129 lattice with 18.6 µm spacing.

The results show successful reconstruction of the phase vortex where the amplitude is not nearly zero. The reconstructed vortex is slightly rotated compared to the ground-truth due to a constant phase shift. Since there is no separate reference wave, constant phase shifts are not measurable and hold no semantic meaning, and hence they can be ignored in practical applications. The amplitude reconstruction is noisier but does capture the overall shape. It is worth noting that 2π phase discontinuities in phase vortices make reconstruction from wavefront sensor images a hard problem; specialized wavefront sensing reconstruction algorithms [22,23] or prior knowledge about the field [11] is usually required, whereas our approach made no assumptions about the field.

To verify our reconstruction method experimentally, we chose to image a 50 µm polystyrene bead embedded in ethylene glycol through an infinity-corrected microscope with an Olympus 40×/0.75NA microscope objective. Light from a light emitting diode (LED) illuminated the specimen after passing through a 540-nm-bandpass filter of 10-nm-bandwidth, and both field and aperture stops in the microscope were fully stopped down to simulate coherent illumination. A Thorlabs WFS150-7AR wavefront sensor with 150 µm circular lenslets was placed at the intermediate image plane, and 1000×1000 pixels were taken from each image. The wavefront sensor was placed on a manual stage to enable taking

amplitude   optical thickness (waves)

optical thickness of cross section
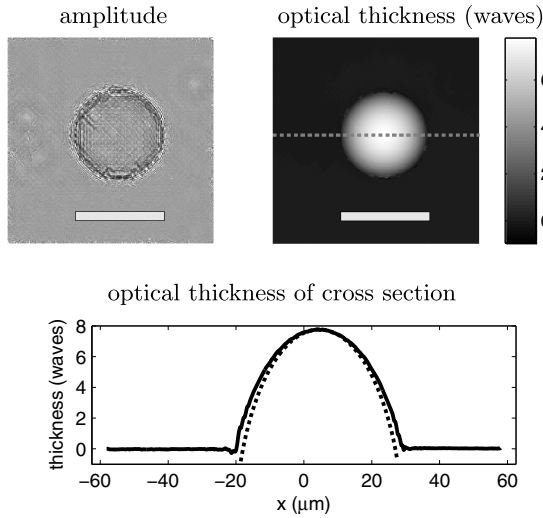
Fig. 4.   Recovered amplitude and unwrapped phase of a 50 μm polystyrene bead embedded in ethylene glycol. Lighter shading corresponds to higher amplitude and optical path length. Scale bar is 50 μm. The solid curve in the bottom graph shows a cross-section (along the dotted line in the phase image) of the unwrapped optical path length, whereas the dashed curve shows the expected optical path length.

images at two positions, with a transverse translation of 75 μm along each axis of the lens array lattice between the two.

First, a set of 16 images with the illumination turned off were captured to calibrate the black level. Then, for each stage position, 16 images were captured to obtain a mean and variance; black level calibration was done by subtracting the black level mean from the captured mean and adding the black level variance to the captured variance (to account for noise in the black level measurements). These two sets of means and variances were then used as input to our modified FFD. To properly simulate the optical system and account for illumination nonuniformities, a similar set of images were captured of a blank slide, their reconstruction result used as a mask in the forward model for the actual specimen. Both reconstructions were run for 1000 iterations, with field specified by a 330×330 lattice with 358-nm spacing. The recovered amplitude and phase are shown in Fig. 4; phase unwrapping was performed using the Constantini method [24]. A plot of the merit function value shows convergence within 1000 iterations in Fig. 5.
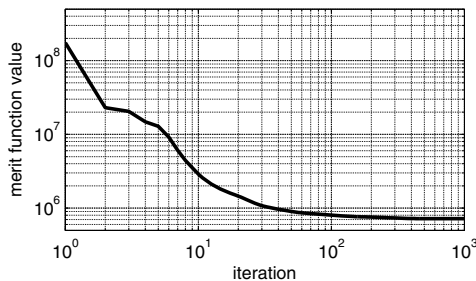
The amplitude and phase images show that the shape of the bead was reconstructed with good fidelity, although there are several artifacts present. The periodic artifacts in the amplitude image are likely due to misalignment of the wavefront sensor as well as mischaracterization of the aberrations in the lenslets. Furthermore, there appear to be artifacts along the edge of the sphere, most prominently seen in the amplitude image. Since the lens array has a focal length of approximately 5.1 mm, the maximum NA at 40× that the lens array can accommodate without crosstalk across lenslets is approximately $75/5100 \times 40 \approx 0.59$, which is smaller than the 0.75 NA of the objective used. Thus, these errors are most likely due to cross talk.

A cross-section of the unwrapped optical path length is shown in the bottom graph in Fig. 4. For comparison, the optical thickness of an ideal bead (with 1.59 and 1.44 used as the index of refraction for polystyrene and ethylene glycol, respectively) is shown as a dashed curve, truncated such that the wavefront curvature does not exceed the NA of the objective. The reconstruction matches the comparison curve quite well, and slight differences between the two curves may be due to diffraction or inaccurate index of refraction values for the comparison curve.

A human cheek cell was imaged similarly, with the field represented as a 222×222 lattice with 464 nm spacing. The resulting amplitude and phase are shown in Fig. 6, and a convergence plot is shown in Fig. 7. The optically thicker nucleus is clearly visible, although some small diagonally oriented artifacts are present.

It is worth noting that the mathematical form of the forward problem in our formulation is quite similar to ptychography—for a flat amplitude-phase specimen, the image formed by a single wavefront sensor lenslet

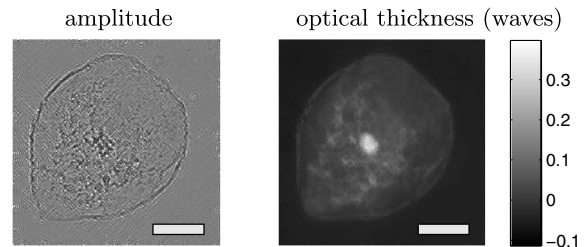amplitude   optical thickness (waves)

Fig. 6.   Recovered amplitude and unwrapped phase of a cheek cell placed between two cover slips. Lighter shading corresponds to higher amplitude and optical path length. Scale bar is 25 μm.

Fig. 5.   Log–log plot of the merit function value as a function of iteration number shows convergence within 1000 iterations for the 50 μm bead specimen.
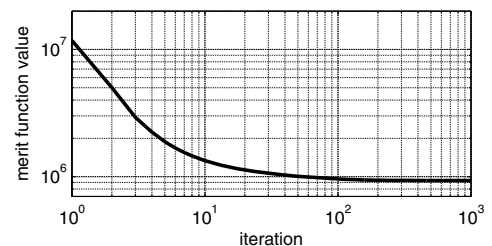
Fig. 7.   Log–log plot of the merit function value as a function of iteration number shows convergence within 1000 iterations for the cheek cell specimen.

provides the same information as the far field of a probe beam with the same shape and position as the lenslet. As we increase the number of shifted images, our measurement data quite obviously become exactly ptychography; we require less scanning, albeit at the cost of having to deal with crosstalk and additional calibration. Increasing the number of shifts also generates more redundancy in the reconstruction (at the limit, the problem becomes the recovery of a two-dimensional data set from a four-dimensional set of measurements), making the problem less ill-posed at the cost of less light per measurement, assuming a fixed photon budget. A more thorough study into this trade-off could lead to practical guidelines regarding the optimum number of shifts. Furthermore, due to the mathematical similarity between wavefront sensing and ptychography, it would be worth investigating the use of modified FFD to process ptychographic data, or even data from other phase imaging methods such as TIE. Lastly, since the wavefront sensor images a smoothed Wigner distribution [25,26], it might be promising to use FFD to recover partially coherent fields from wavefront sensor data.

References

1. J. H. Bruning, D. R. Herriott, J. E. Gallagher, D. P. Rosenfeld, A. D. White, and D. J. Brangaccio, Appl. Opt. **13**, 2693 (1974).
2. L. M. Frantz, A. A. Sawchuk, and W. von der Ohe, Appl. Opt. **18**, 3301 (1979).
3. C. M. Vest, *Holographic Interferometry* (Wiley, 1979).
4. P. Hariharan, B. Oreb, and N. Brown, Opt. Commun. **41**, 393 (1982).
5. I. Yamaguchi and T. Zhang, Opt. Lett. **22**, 1268 (1997).
6. E. Cuche, F. Bevilacqua, and C. Depeursinge, Opt. Lett. **24**, 291 (1999).
7. J. Hartmann, Z. Instrumentenkd **20**, 17 and 47 (1900).
8. R. V. Shack and B. C. Platt, in *Program of the 1971 Spring Meeting of the Optical Society of America* (Optical Society of America, 1971), p. 656.
9. A. Polo, V. Kutchoukov, F. Bociort, S. Pereira, and H. Urbach, Opt. Express **20**, 7822 (2012).
10. C. Li, B. Li, and S. Zhang, Appl. Opt. **53**, 618 (2014).
11. B. Stoklasa, L. Motka, J. Rehacek, Z. Hradil, and L. Sánchez-Soto, Nat. Commun. **5**, 3275 (2014).
12. R. W. Gerchberg and W. O. Saxton, Optik **35**, 237 (1972).
13. J. R. Fienup, Appl. Opt. **21**, 2758 (1982).
14. M. R. Teague, J. Opt. Soc. Am. **73**, 1434 (1983).
15. N. Streibl, Opt. Commun. **49**, 6 (1984).
16. J. Rodenburg, Ultramicroscopy **27**, 413 (1989).
17. J. Rodenburg, Adv. Imaging Electron Phys. **150**, 87 (2008).
18. A. M. Maiden, J. M. Rodenburg, and M. J. Humphry, Opt. Lett. **35**, 2585 (2010).
19. M. R. Arnison, K. G. Larkin, C. J. R. Sheppard, N. I. Smith, and C. J. Cogswell, J. Microsc. **214**, 7 (2004).
20. Z. Zhang, Z. Chen, S. Rehman, and G. Barbastathis, Opt. Express **21**, 5759 (2013).
21. E. Karimi, G. Zito, B. Piccirillo, L. Marrucci, and E. Santamato, Opt. Lett. **32**, 3053 (2007).
22. D. L. Fried, Opt. Commun. **200**, 43 (2001).
23. F. A. Starikov, G. G. Kochemasov, S. M. Kulikov, A. N. Manachinsky, N. V. Maslov, A. V. Ogorodnikov, S. A. Sukharev, V. P. Aksenov, I. V. Izmailov, F. Y. Kanev, V. V. Atuchin, and I. S. Soldatenkov, Opt. Lett. **32**, 2291 (2007).
24. M. Costantini, IEEE Trans. Geosci. Remote Sens. **36**, 813 (1998).
25. Z. Zhang and M. Levoy, in *IEEE International Conference on Computational Photography (ICCP)* (IEEE, 2009), p. 1.
26. L. Tian, Z. Zhang, J. C. Petruccelli, and G. Barbastathis, Opt. Express **21**, 10511 (2013).